Enhanced Phase Mixing of Torsional Alfvén Waves in Stratified and Divergent Solar Coronal Structures, Paper II: Nonlinear Simulations

C. Boocock[1]* [iD] and D. Tsiklauri[2] [iD]

[1]*Queen Mary University of London, Mile End Road, London E1 4NS, UK,*
[2]*School of Science and Technology, University of Georgia, 77a Kostava Street, 0171 Tbilisi, Georgia*

ABSTRACT

We use MHD simulations to detect the nonlinear effects of torsional Alfvén wave propagation in a potential magnetic field with exponentially divergent field lines, embedded in a stratified solar corona. In Paper I we considered solutions to the linearised governing equations torsional Alfvén wave propagation and showed, using a finite difference solver we developed named *WiggleWave*, that in certain scenarios wave damping is stronger than what would be predicted by our analytic solutions. In this paper we consider whether damping would be further enhanced by the presence of nonlinear effects. We begin by deriving the nonlinear governing equations for torsional Alfvén wave propagation and identifying the terms that cause coupling to magnetosonic perturbations. We then compare simulation outputs from an MHD solver called *Lare3d*, which solves the full set of nonlinear MHD equations, to the outputs from *WiggleWave* to detect nonlinear effects such as: the excitation of magnetosonic waves by the Alfvén wave, self-interaction of the Alfvén wave through coupling to the induced magnetosonic waves, and the formation of shock waves higher in the atmosphere caused by the steepening of these compressive perturbations. We suggest that the presence of these nonlinear effects in the solar corona would lead to Alfvén wave heating that exceeds the expectation from the phase mixing alone.

Key words: (magnetohydrodynamics) MHD – Plasmas – Waves – Sun: corona – Sun: oscillations

1 INTRODUCTION

In this paper we consider the propagation and enhanced phase mixing of torsional Alfvén waves in open structures in the solar corona with exponentially diverging magnetic field lines and a gravitationally stratified atmosphere. For a long time wave-based heating has been considered as a mechanism to heat the solar corona (Ofman 2005). A large variety of magnetic waves have been detected in the corona (Parnell & De Moortel 2012). In particular torsional Alfvén waves have recently been detected in the photosphere (Stangalini et al. 2021) and it has been shown in (Soler et al. 2017) that torsional Alfvén waves of intermediate frequencies are able to penetrate to the corona, and that expanding flux tubes favour this transmission. Torsional Alfvén waves can also be generated in the corona when the magnetic field relaxes following a solar flare (Fletcher & Hudson 2008).

Although Alfvén waves are viable transporters of non-thermal energy to solar corona they are difficult to dissipate due to the high conductivity of the corona, (Tsiklauri 2009). Dissipation must therefore occur over small length scales typically generated by in inhomogeneities in the corona, (De Moortel et al. 2008). Phase mixing is a mechanism first proposed by (Heyvaerts & Priest 1983) that increases the viscous and ohmic dissipation of Alfvén waves in the solar corona. When Alfvén waves on neighboring magnetic surfaces propagate at different speeds they move out of phase with one another

leading to strong gradients transverse to the direction of propagation, thus increasing the effect of viscous or resistive heating in the plasma.

Enhanced phase mixing occurs in divergent magnetic structures such as those that are found in open field regions or at the base of large (50-100 Mm height) coronal loops. The decrease of magnetic field strength along field lines means a decreasing Alfvén velocity that in turn reduces the wavelength of propagating Alfvén waves and ultimately enhances the effect of phase mixing. Conversely a stratified density gradient has the opposite effect, by increasing the Alfvén velocity in the direction of propagation, wavelengths are increased and the effect of phase mixing is diminished (Smith et al. 2007).

In Paper I we considered at solutions to the linearised governing equations for the propagation of torsional Alfvén waves in a potential magnetic field with exponentially divergent field lines, embedded in a stratified solar corona. We used the WKB approximation to derive an analytic solution for Alfvén wave propagation and damping due to enhanced phase mixing. We also developed an IDL code, *TAWAS* (https://github.com/calboo/TAWAS), to calculate this solution over a coordinate grid. We then developed a finite difference solver *Wigglewave* (https://github.com/calboo/Wigglewave) that solves the linearised governing equations directly.

By comparing the outputs from these two codes we showed that the analytic solution is accurate within the limits of the WKB approximation, but beyond the limits of the WKB approximation the analytic formula under-reports the effect of Alfvén wave damping. We also showed that torsional Alfvén waves driven from the base of the corona can be fully dissipated within 100 Mm if the field is

---

* E-mail: c.boocock@qmul.ac.uk

magnetic field lines are highly divergent, the wave period is low and a high value of anomalous kinematic viscosity is applied. These conditions could be relaxed if additional physical effects are considered such as pressure, three-dimensionality and nonlinearity (Smith et al. 2007). In this paper we consider the effects of nonlinearity on the propagation and enhanced phase mixing of torsional Alfvén waves. We do this by using an MHD solver called *Lare3d*, (Arber et al. 2001), to simulate torsional Alfvén wave propagation using the full nonlinear MHD equations.

In order to detect the effects nonlinearity we compare the outputs from *Lare3d* to those from *Wigglewave*. We also compare the outputs from several *Lare3d* simulations with different amplitudes for the driving Alfvén wave. We are able to detect effects such as the excitation of magnetosonic waves by Alfvén wave phase mixing, as described in (Nakariakov et al. 1997) and simulated in (Shestov et al. 2017) who demonstrate the excitation of both fast and slow modes; the trapping of magnetosonic waves due to refraction within the tube structure, as mentioned in (Roberts 2000); the generation of compressive perturbations associated with the magnetosonic waves, as identified in (Ofman et al. 1999) and the steepening of these perturbations into shock waves as discussed in (Malara et al. 1996).

Although we are unable to directly measure Alfvén wave damping from our *Lare3d* simulation outputs we can infer from previous research that the emergence of nonlinear effects, such as coupling to magnetosonic waves and shock formation, provide an alternative, and often more efficient, mechanism for Alfvén wave dissipation and viscous heating (Arber et al. 2016), (Malara et al. 2000), (Malara et al. 1996).

In section 2 we derive the nonlinear equations for the propagation of torsional Alfvén waves in an axisymmetric potential magnetic field. Using these we can see how the linearised equations were originally derived and we can identify the nonlinear terms that give rise to additional physical effects. In section 3 we will see these effects arising in 3D MHD simulations performed using *Lare3d*.

2 NONLINEAR EFFECTS OF TORSIONAL ALFVÉN WAVES PROPAGATING IN A POTENTIAL AXISYMMETRIC MAGNETIC FIELD

In this section we will show mathematically which terms in the nonlinear MHD equations cause the system to deviate from purely torsional and incompressible perturbations and which physical effects these terms correspond to. To do this we derive the full nonlinear equations for torsional Alfvén waves propagating in a potential axisymmetric magnetic field and identify which terms are nonlinear and how they effect the system.

We demonstrate how torsional Alfvén waves propagating in a potential axisymmetric magnetic field can excite magnetosonic waves which can then interact back with the Alfvén waves and cause perturbations to the density. We begin with the cold ($\beta = 0$), ideal (zero viscosity, zero resistivity) MHD equations,

$$\rho \frac{\partial \mathbf{v}}{\partial t} + \rho (\mathbf{v} \cdot \nabla)\mathbf{v} = -\frac{1}{\mu_0} \mathbf{B} \times (\nabla \times \mathbf{B}), \tag{1}$$

$$\frac{\partial \mathbf{B}}{\partial t} = \nabla \times (\mathbf{v} \times \mathbf{B}), \tag{2}$$

$$\frac{\partial \rho}{\partial t} + \nabla \cdot (\rho \mathbf{v}) = 0, \tag{3}$$

$$\nabla \cdot \mathbf{B} = 0. \tag{4}$$

We have omitted the inclusion of viscosity in the momentum equation for conciseness and simplicity, furthermore as the kinematic viscosity ν is constant, the viscosity term, $\nu\nabla^2 v$, is linear in v so would be unaffected by the eventual linearisation of these equations. We consider these MHD equations in cylindrical coordinates (r, z, θ) and with the condition of axisymmetry ($\partial/\partial\theta = 0$), the resultant components of the MHD equations are shown in appendix A. We then consider perturbations to an equilibrium state, $\mathbf{v_0} = \mathbf{0}$, $\mathbf{B_0} = (B_{0r}, 0, B_{0z})$ and $\rho_0 = \rho_0(r, z)$, that take the form,

$$\begin{aligned} \rho &= \rho_0 + \rho', \\ \mathbf{v} &= \mathbf{0} + \mathbf{v}, \\ \mathbf{B} &= \mathbf{B_0} + \mathbf{b}, \end{aligned} \tag{5}$$

where our equilibrium magnetic field is a potential field such that,

$$\nabla \times \mathbf{B_0} = \begin{pmatrix} 0 \\ \partial_z B_{0r} - \partial_r B_{0z} \\ 0 \end{pmatrix} = \mathbf{0}. \tag{6}$$

The resultant nonlinear equations for these perturbations are also given in appendix A with the linear and nonlinear terms shown separately. Looking at these equations, we can associate the variables v_θ and b_θ with Alfvén waves and the variables v_r, v_z, b_r, b_z with magnetosonic waves.

We can see that the nonlinear terms, which correspond to the evolution equations for v_r, v_z, b_r, b_z, contain terms with either two magnetosonic variables or two Alfvén wave variables, indicating that the magnetosonic waves can be excited by Alfvén waves and can self-interact.

In contrast the nonlinear terms that correspond to the evolution equations for v_θ and b_θ, contain only terms with an Alfvén wave variable and a magnetosonic variable, indicating that they cannot be excited by magnetosonic waves but can interact with the induced magnetosonic waves. In other words, the torsional Alfvén waves can only self-interact in the presence of magnetosonic perturbations (Vasheghani Farahani et al. 2012).

If the nonlinear terms in these equations are ignored, and we imagine a point in time where perturbations are purely torsional, such that v_r, b_r, v_z, b_z and $\rho' = 0$, then the system stays incompressible and the perturbations remain purely torsional. The equations for this system are given in appendix B. By simplifying the equations for v_θ and b_θ and reintroducing the viscosity term, we arrive back at the linearised governing equations for torsional Alfvén wave propagation presented in Paper I and shown below in eqs. (7) and (8), this transformation is also shown explicitly in appendix B.

$$\rho \frac{\partial v}{\partial t} = \frac{1}{r\mu_0} (\mathbf{B_0} \cdot \nabla(rb)) + \frac{1}{r} \frac{\partial}{\partial r} \left(\rho\nu r \frac{\partial v}{\partial r} \right) + \frac{\partial}{\partial z} \left(\rho\nu \frac{\partial v}{\partial z} \right), \tag{7}$$

$$\frac{\partial b}{\partial t} = r\mathbf{B_0} \cdot \nabla \left(\frac{v}{r} \right). \tag{8}$$

Now let us see what happens to an initially incompressible system with purely torsional perturbations when nonlinear effects are included. We consider a time at which v_r, b_r, v_z, b_z and $\rho' = 0$ but this time we include all of the nonlinear terms. This gives us,

$$\rho_0 \partial_t v_r = -\frac{1}{\mu_0} b_\theta \partial_r b_\theta - \frac{\rho_0 v_\theta^2}{r} - \frac{1}{\mu_0} \frac{b_\theta^2}{r}, \tag{9}$$

$$\rho_0 \partial_t v_\theta = \frac{1}{\mu_0} \left(\frac{B_{0r}}{r} \partial_r (r b_\theta) + B_{0z} \partial_z b_\theta \right), \tag{10}$$

$$\rho_0 \partial_t v_z = -\frac{1}{\mu_0} b_\theta \partial_z b_\theta, \tag{11}$$

$$\partial_t b_r = 0, \tag{12}$$

$$\partial_t b_\theta = \partial_z (B_{0z} v_\theta) + \partial_r (B_{0r} v_\theta), \tag{13}$$

$$\partial_t b_z = 0, \tag{14}$$

$$\partial_t \rho' = 0. \tag{15}$$

This nonlinear system will quickly evolve so that v_r and v_z are no longer zero which will lead to perturbations in b_r and b_z and cause the system to become compressible.

Looking at the momentum equations for v_r and v_z eqs. (9) and (11) we can see that the nonlinear generation of magnetosonic waves is caused by: the varying magnetic pressure of the Alfvén wave, $\nabla(\mathbf{b}^2/2\mu_0)$, also known as the ponderomotive force (Hollweg 1971; Tikhonchuk et al. 1995); the magnetic tension force $(\mathbf{b} \cdot \nabla)\mathbf{b}/\mu_0$ and centrifugal force, $\rho_0(\mathbf{v}\cdot\nabla)\mathbf{v}$. When we expand these terms we can see how they each appear in the momentum equations eqs. (9) and (11),

$$-\frac{1}{2\mu_0}\nabla\mathbf{b}^2 = -\frac{1}{\mu_0}\mathbf{b}\nabla\mathbf{b} = \mathbf{f_1}, \quad \text{where} \quad \mathbf{f_1} = \begin{pmatrix} -\frac{b_\theta}{\mu_0}\partial_r b_\theta \\ 0 \\ -\frac{b_\theta}{\mu_0}\partial_z b_\theta \end{pmatrix}, \tag{16}$$

$$\frac{1}{\mu_0}(\mathbf{b}\cdot\nabla)\mathbf{b} = \mathbf{f_2}, \quad \text{where} \quad \mathbf{f_2} = \begin{pmatrix} -\frac{1}{\mu_0}\frac{b_\theta^2}{r} \\ 0 \\ 0 \end{pmatrix}, \tag{17}$$

$$\rho_0(\mathbf{v}\cdot\nabla)\mathbf{v} = \mathbf{f_3}, \quad \text{where} \quad \mathbf{f_3} = \begin{pmatrix} -\rho_0\frac{v_\theta^2}{r} \\ 0 \\ 0 \end{pmatrix}. \tag{18}$$

The ponderomotive force is present for the propagation of shear Alfvén waves but the magnetic tension and centrifugal forces are unique to torsional Alfvén waves. It is these three nonlinear forces that cause the generation of magnetosonic waves which can subsequently interact with the torsional Alfvén wave. In (Vasheghani Farahani et al. 2012), which considers the dynamics of torsional Alfvén waves in a uniform magnetic flux tube using the second-order thin flux tube approximation, we see the same nonlinear terms appearing in the derived wave equation. Furthermore (Vasheghani Farahani et al. 2012) also concludes that the nonlinear self-interaction of the Alfvén waves is caused by interaction of the waves with nonlinearly induced, compressive perturbations.

In section 3 we use MHD simulations to explore the effects of these nonlinear forces on the propagation of torsional Alfvén waves, the excitation of magnetosonic waves and the generation of shocks.

3 SIMULATIONS

Lare3d (Arber et al. 2001) is a Lagrangian remap code that solves the full viscous MHD equations over a 3D staggered Cartesian grid. In Paper I we used our finite difference solver *WiggleWave* to simulate solutions for the linearised governing equations eqs. (7) and (8) for the propagation of torsional Alfvén waves. By comparing the simulation outputs from *Lare3d* to those from *WiggleWave* we can detect nonlinear effects. The numerical setup that we use for our *Lare3d* and *WiggleWave* simulations is as the same setup we used for our *WiggleWave* simulations in Paper I and is briefly described in the following subsection for clarity.

3.1 Numerical Setup

The equilibrium magnetic field is potential, axisymmetric and has no azimuthal component. It is defined by it's radial and vertical components as,

$$B_r = B_0 e^{-z/H} J_1(r/H), \qquad B_z = B_0 e^{-z/H} J_0(r/H), \tag{19}$$

where H is the magnetic scale height, J_0 and J_1 are Bessel functions of the first kind and of zero and first order respectively. In *Lare3d* we must define this field using Cartesian magnetic field components which are,

$$B_x = \frac{B_0 x}{r} e^{-z/H} J_1(r/H), \tag{20}$$

$$B_y = \frac{B_0 y}{r} e^{-z/H} J_1(r/H), \tag{21}$$

$$B_z = B_0 e^{-z/H} J_0(r/H), \tag{22}$$

We also calculate magnetic field coordinates as we need these to define our density structure. The magnetic coordinates ϕ and ψ are defined using the radius r,

$$r = \sqrt{x^2 + y^2} \tag{23}$$

$$\phi = -H e^{-z/H} J_0(r/H) \tag{24}$$

$$\psi = r e^{-z/H} J_1(r/H). \tag{25}$$

We can now define the gravitationally stratified density structure as follows,

$$\rho = \hat{\rho}(\psi) e^{-z/H_\rho} = \hat{\rho}(\psi) e^{-\alpha z/H}, \tag{26}$$

where the density scale height $H_\rho = k_B T/mg$, k_B is Boltzmann's constant, T is the temperature and is constant, $m \approx 0.6 m_P$, where m_P is the proton mass, g is the solar surface gravity, $\alpha = H/H_\rho$ and $\hat{\rho}(\psi)$ is an arbitrary function that defines the density variation across magnetic field lines. We use $\hat{\rho}(\psi)$ to define a central higher density tube that is enclosed within the field line defined by $\psi = \psi_b$. The field line $\psi = \psi_b$ intersects the lower boundary at radius r_0 which defines the width of the tube. We define $\hat{\rho}(\psi)$ to be,

$$\hat{\rho}(\psi) = \frac{\rho_0}{\zeta} \begin{cases} 1 + (\zeta - 1)(1 - \psi/\psi_b)^2, & \psi \le \psi_b \\ 1, & \psi \ge \psi_b \end{cases} \tag{27}$$

where ζ is the density contrast between the centre and exterior of the magnetic tube $\hat{\rho}(0)/\hat{\rho}(\psi_b)$. The transverse density and Alfvén speed profiles along the lower boundary $z = 0$ are shown in fig. 1 and the Alfvén speed across the whole domain is shown in fig. 2.
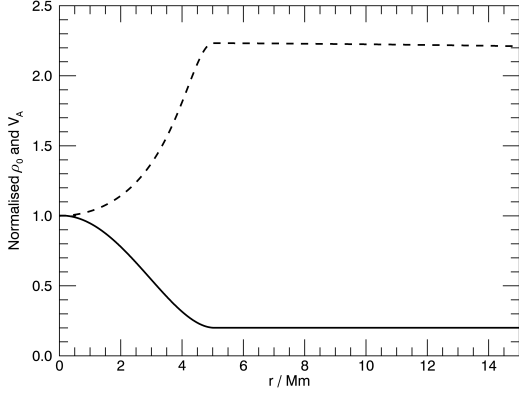
Figure 1. A graph showing how the normalised equilibrium density ρ_0 (solid line) and normalised Alfvén speed V_A (dashed line) change with radius along the lower boundary of the domain i.e. for $z = 0$. Note that the density and Alfvén speed are constant outside the flux tube and are structured within the central flux tube, rather than reaching a plateau.
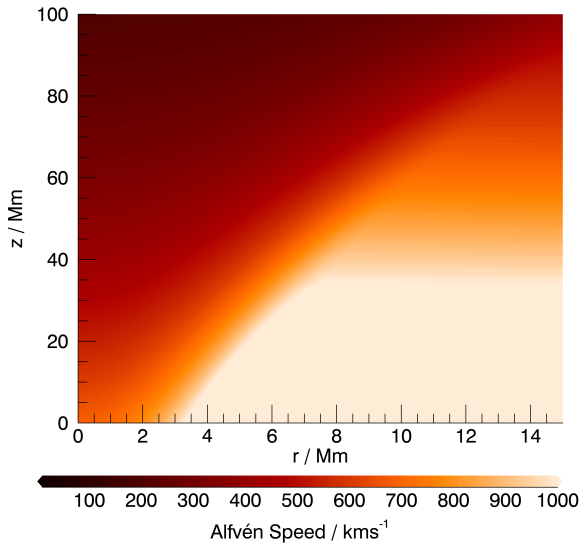

Figure 2. A colour contour of the Alfvén speed across the computational domain. The azimuthal direction is ignored due to the condition of axisymmetry. The Alfvén speed varies both transversely across field lines i.e with ψ and also exponentially with height z.

Finally we define our wave driving by prescribing the velocity and magnetic field at the lower boundary, which we approximate as a flat magnetic surface. The wave driving for both v_θ and b_θ, within the tube boundary $r = r_0$ are given by,

$$v = u_0 \frac{r}{r_0} \left(1 - \left(\frac{r}{r_0}\right)^2\right) \sin\left(\omega\left(\frac{z}{V_A} - t\right)\right), \tag{28}$$

$$b = -u_0 \frac{r}{r_0} \left(1 - \left(\frac{r}{r_0}\right)^2\right) \sin\left(\omega\left(\frac{z}{V_A} - t\right)\right) \sqrt{\mu_0 \rho}. \tag{29}$$

In *Lare3d* we must define this driving in terms of v_x, v_y, b_x and b_y the equivalent driving is then defined by,

$$v_x = -u_0 \frac{y}{r_0} \left(1 - \left(\frac{r}{r_0}\right)^2\right) \sin\left(\omega\left(\frac{z}{V_A} - t\right)\right), \tag{30}$$

$$v_y = u_0 \frac{x}{r_0} \left(1 - \left(\frac{r}{r_0}\right)^2\right) \sin\left(\omega\left(\frac{z}{V_A} - t\right)\right), \tag{31}$$

$$b_x = -u_0 \frac{y}{r_0} \left(1 - \left(\frac{r}{r_0}\right)^2\right) \sin\left(\omega\left(\frac{z}{V_A} - t\right)\right), \tag{32}$$

$$b_y = u_0 \frac{x}{r_0} \left(1 - \left(\frac{r}{r_0}\right)^2\right) \sin\left(\omega\left(\frac{z}{V_A} - t\right)\right). \tag{33}$$

Considering propagation of Alfvén waves in a typical coronal plume or divergent coronal loop structures, we set our characteristic field strength as $B_0 = 0.001$ T, and our characteristic density as $\rho_0 = 1.66 \times 10^{-12}$ kg m^{-3} (which corresponds to a number density of approximately $n_0 = 1 \times 10^{15}$ m^{-3}). This gives us a characteristic Alfvén speed of $V_0 \approx 700$ km s^{-1}. We fix the initial tube radius to be $r_0 = 5$ Mm and the density contrast to be $\zeta = 5$.

For the simulations in this paper we only consider the scenario for which the magnetic scale height is $H = 50$ Mm, the density scale height is $H_\rho = 50$ Mm (corresponding to a coronal temperature of around 1 MK, see (Aschwanden 2004)), the kinematic viscosity is $\nu = 5 \times 10^7$ m^{2}s^{-1} and the period of wave driving is $T = 60$ s.

For our initial comparison of *Lare3d* and *WiggleWave* simulations we set the amplitude of our Alfvén wave driving at the lower boundary using a value of $u_0 = 100$ km s^{-1} this corresponds to a maximum value of about 40 km s^{-1} (approximately 5% of the local Alfvén speed). These values are what we might expect in the corona based on (Banerjee et al. 1998) and (Doyle et al. 1999).

For our *WiggleWave* simulation the grid resolution used over the domain is set to 500×2000, in the r and z directions respectively. *Lare3d* uses a Cartesian grid so we set our resolution to $1000 \times 1000 \times 2000$, in x, y and z directions, to allow a direct comparison with the *WiggleWave* simulation. In both *Lare3d* and *WiggleWave* simulations exponential damping regions were included for the upper vertical and outer radial boundaries when necessary, to prevent wave reflection from these boundaries.

3.2 Simulation Comparison

The outputs that we will analyse from our *Lare3d* simulations are from a simulation time of only 578 s. The reason for this is that during these simulations the density can dramatically increase, as we will discuss below, this causes the timestep to decrease and slows down the simulation exponentially due to the CFL condition, (Kwatra et al. 2009).

The outputs from *Lare3d* are the density ρ, velocity field components, v_x, v_y, v_z, magnetic field components, b_x, b_y, b_z and pressure P. When comparing outputs we present only the velocity components of the wave but the magnetic field perturbations have also been checked and display the same nonlinear effects. We can convert the Cartesian velocity components from *Lare3d* into cylindrical equivalents v_r and v_θ using the formulae,

$$v_r = \frac{\partial r}{\partial t} = \frac{x v_x + y v_y}{\sqrt{x^2 + y^2}} \tag{34}$$

$$v_\theta = r\frac{\partial \theta}{\partial t} = \frac{x v_y - y v_x}{\sqrt{x^2 + y^2}} \tag{35}$$
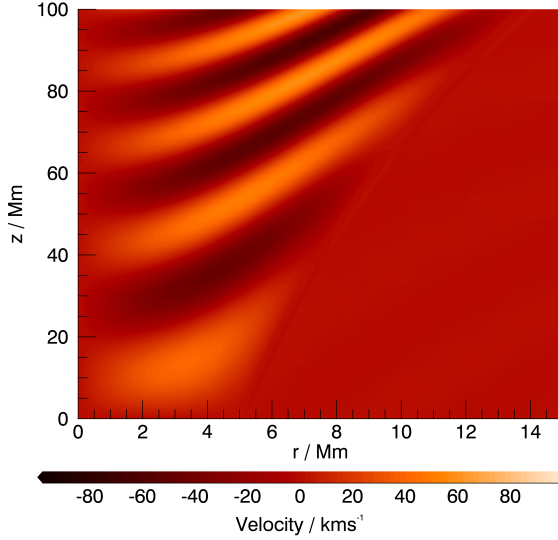
Figure 3. A graph of v_θ, over the half plane $y = 0$, $x > 0$, from the *Wigglewave* simulation of the scenario with $H = 50$ Mm, $H_\rho = 50$ Mm, $\nu = 5 \times 10^7$ m^{2}s^{-1} and $T = 60$ s. We can see the smooth wave fronts of the torsional Alfvén wave propagating.
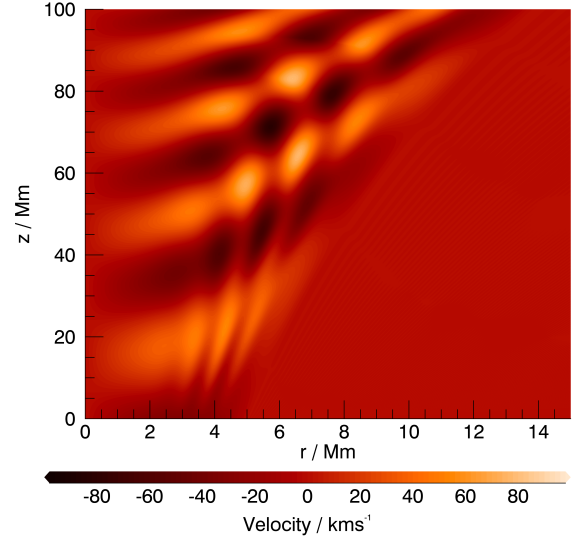

Figure 4. A graph of v_θ, over the half plane $y = 0$, $x > 0$, from the *Lare3d* simulation of the scenario with $H = 50$ Mm, $H_\rho = 50$ Mm, $\nu = 5 \times 10^7$ m^{2}s^{-1} and $T = 60$ s. We can see a fringed pattern superimposed on the wave fronts of the torsional Alfvén wave that bends inwards due to refraction that is caused by nonlinear self-interaction.

v_z is unchanged between Cartesian and cylindrical coordinate systems. When comparing outputs we can use the axisymmetry of the outputs to our advantage. By looking at velocities across the plane $y = 0$, the we can equate $x = r$, $v_x = v_r$ and $v_y = v_\theta$.

Contours of v_θ are shown for the *WiggleWave* and *Lare3d* simulations in figs. 3 and 4 respectively. We can see that both simulations show the expected wavefront pattern due to the propagation of the Alfvén wave but the *Lare3d* outputs also show a fringed pattern that is superimposed. We will see below that this effect is nonlinear and diminishes at lower amplitudes and that the cause of this effect is nonlinear coupling of the torsional Alfvén wave with magnetosonic perturbations.

These magnetosonic waves are themselves excited nonlinearly by the Alfvén waves. The nonlinear excitation of magnetosonic waves by the phase mixing of Alfvén wave is a well known phenomena. It is explained in (Nakariakov et al. 1997) that the phase mixing of shear Alfvén waves can excite magnetosonic modes. The nonlinear forces responsible for the generation of manetosonic waves are identified in section 2.

The magnetosonic waves can be identified by looking at perturbations to v_r and v_z in the *Lare3d* simulation outputs. Perturbations to v_r and v_z are not calculated in *WiggleWave* as they do not arise in the linear system of equations solved by the code. Perturbations to v_θ, v_r and v_z from our *Lare3d* outputs are shown in fig. 5. The presence of perturbations to v_r and v_z is a clear indicator of magnetosonic waves.

Once generated, the magnetosonic waves become trapped inside the central flux tube due to the transverse density structuring. The enhanced density within the flux tube means that the Alfvén velocity is lower inside the flux tube than outside. This causes the waves to refract within the tube which acts a type of waveguide (Roberts 2000; Ofman 2010). This refraction can clearly be seen in figs. 4 and 5.

To confirm the nonlinear nature of the generated magnetosonic waves we performed two additional *Lare3d* runs with the same parameters but smaller amplitudes. In these two runs we set $u_0 = 10$ km s^{-1} and $u_0 = 1$ km s^{-1}. In fig. 6 we can see contours of v_θ, v_r and v_z for the run with $u_0 = 10$ km s^{-1}. Comparing these contours to the

ones in fig. 5 we can see that, besides the amplitudes being smaller, the interference fringes in the v_θ contour are much less pronounced in the lower amplitude run. Furthermore whilst the amplitude of v_θ is different by a factor of only 10 between runs, the amplitudes of v_r and v_z are different by a factor of approximately 100, indicating the nonlinear nature of magnetosonic wave excitement.

This point is clarified in fig. 7 which shows log-log plots of the maximum values for both v_r and v_z against the driving amplitude u_0 across all three simulations. We can see that the slope of these log-log graphs is approximately two, meaning that the amplitude of excited magnetosonic waves scales as roughly the square of the Alfvén wave amplitude. Due to the constraints of the CFL condition it is not possible to tell if the magnetosonic waves in our simulations have, or indeed will, reach a point of saturation due to destructive interference as described in (Tsiklauri, D. et al. 2002, 2001). Nonetheless we might expect this kind of quadratic relationship based on the calculations and simulations for shear Alfvén waves made in (Nakariakov et al. 1997; Botha et al. 2000) and for torsional Alfvén waves in (Shestov et al. 2017).

The mode conversion to magnetosonic waves indirectly provides another mechanism for the Alfvén waves to heat the corona as the generated magnetosonic waves can themselves cause heating through viscous dissipation and shock heating, as discussed in (Antolin & Shibata 2010). The presence of the fringed pattern in v_θ for the *Lare3d* simulations, however, means that we can no longer reliably calculate the wave energy flux from the wave envelope. Despite being unable to measure the damping of the torsional Alfvén waves directly from our outputs, we can detect some very relevant physical effects. In addition to detecting the mode conversion and self-interaction of the Alfvén wave we can also see shock formation caused by the generated magnetosonic modes as discussed in the following subsection.
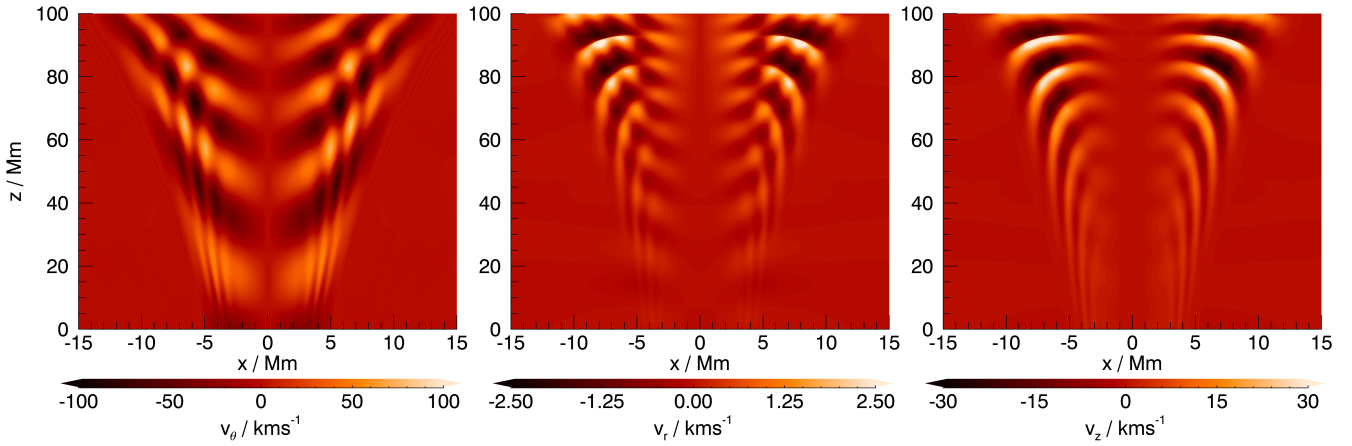
Figure 5. Contour plots of the v_θ (left), v_r (centre) and v_z (right) velocity components, across the plane $y = 0$, from the *Lare3d* simulation with an amplitude $u_0 = 100$ km s^{-1}. Note that whilst the contour range for each plot is different the magnitude of v_z perturbations is of a similar order of magnitude to the v_θ perturbations of the Alfvén wave.
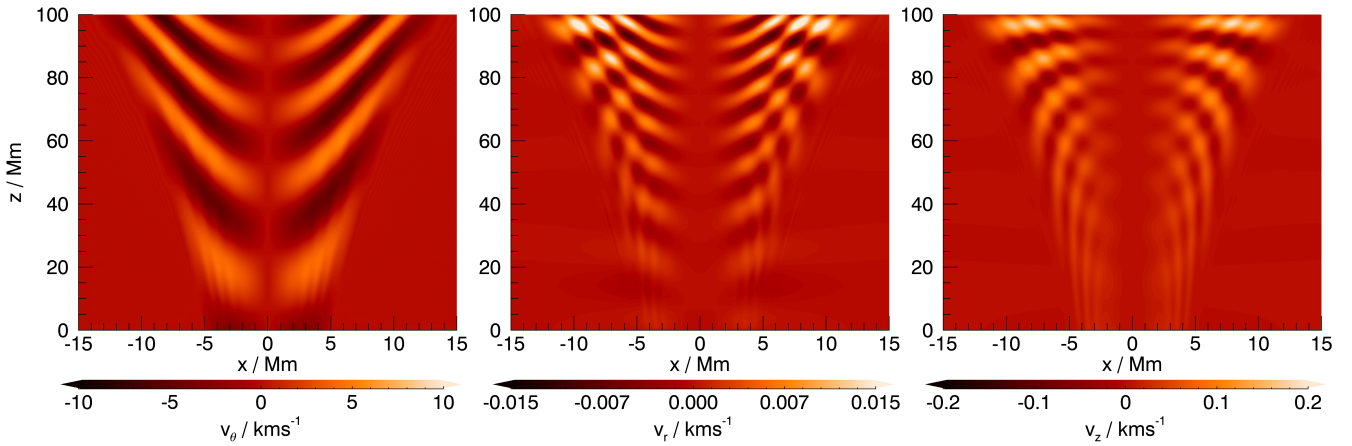

Figure 6. Contour plots of the v_θ (left), v_r (centre) and v_z (right) velocity components, across the plane $y = 0$, from the *Lare3d* simulation with an amplitude $u_0 = 10$ km s^{-1}. Note that the contour range for each plot is different and the magnitude of v_θ Alfvén wave perturbations is much greater than v_r and v_z perturbations of the magnetosonic waves.

3.3 Shock Formation

An important aspect of magnetosonic waves is that they are able to perturb the plasma density. Indeed from eq. (A16) in section 2 we can see that if v_r and v_z are non-zero then the system is no longer incompressible. It is stated in (Malara et al. 1996) that Alfvén waves propagating in an compressive nonuniform medium give rise to compressible perturbations that can steepen into shocks that are extremely efficient at dissipating their energy. In (Arber et al. 2016) it is suggested that ponderomotive coupling of Alfvén waves to slow modes, which subsequently develop into shocks, is the dominant mechanism that Alfvén waves heat the chromosphere.

Here we will look for evidence of shock formation in our *Lare3d* outputs. Shock formation may provide an alternative and possibly more efficient mechanism for Alfvén wave dissipation and one that can potentially be faster than phase mixing (Malara et al. 2000). To detect compressive perturbations and shocks we consider the density profile from our initial *Lare3d* simulation that uses a wave driving

amplitude of $u_0 = 100$ km s^{-1}. Once again we need only consider the density in the plane $y = 0$ due to the axisymmetry of our outputs.

The initial density profile is shown as both as surface plot and a contour in fig. 8 and the density after 578 s of simulation time is shown both as surface plot and a contour in fig. 9. We can see from comparing figs. 8 and 9 that as the Alfvén and magnetosonic waves evolve, compressive waves in the density start to form. These waves are directed along the magnetic field lines rather than across them and can therefore be associated with slow magnetosonic modes. The compressive waves begin to form lower in the corona and increase in amplitude as they propagate higher up. As the waves increase in amplitude they begin to steepen and form shock waves.

Similar waves are mentioned in (Ofman et al. 1999) which describe quasi-periodic compressional waves that increase in amplitude with height being observed within coronal plumes up to about 140 Mm. The simulations in (Ofman et al. 1999) suggest that these waves are outwardly-propagating slow magnetosonic waves that have become trapped and nonlinearly steepen in the plumes, we may be seeing something similar in our Lare3d simulations.
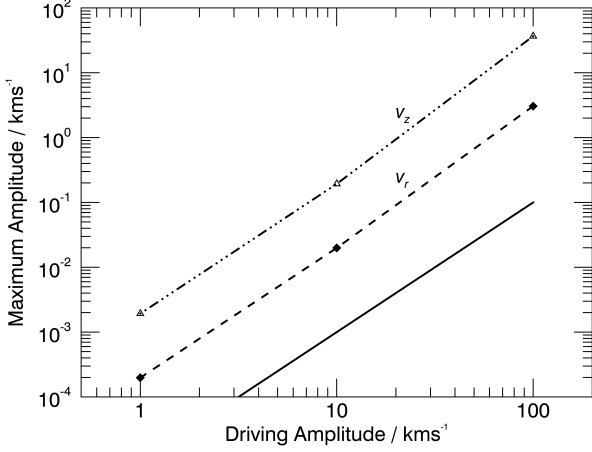
Figure 7. A log-log graph showing the maximum amplitudes of v_r (dashed line with diamond data points) and v_z (dot-dashed line with triangular data points), from Lare3d simulation outputs after a simulation time of 578 s. The three simulations used driving amplitudes $u_0 = 1$, 10 and 100 km s^{-1} as shown on the $x-$ axis. The solid black line is shown for comparison and is an analytic quadratic function of the driving amplitude.

Furthermore both (Kudoh & Shibata 1999) and (Cranmer & Woolsey 2015) describe the nonlinear coupling of Alfvén waves to compressive magnetosonic modes, which then steepen into shocks, as a mechanism for the generation of spicules. This is described as occurring along open magnetic flux tubes such as those found in coronal holes and modelled in our own simulations. Although our simulations take place in the corona rather than the chromosphere it is likely that the same mechanisms are at play.

3.4 Flow Rates

One might expect that the formation of shocks from compressive perturbations would result in an outward flow of plasma from the corona. For this reason we decided to calculate the mass flow rate of plasma through each magnetic surface in the direction of the outward magnetic field. We assume that all of the flow takes place within the central flux tube i.e. for $\psi < \psi_b$. We begin by calculating the plasma velocity directed along magnetic field lines as,

$$\frac{\mathbf{v} \cdot \mathbf{B_0}}{B} = (v_r B_r + v_z B_z)/B. \tag{36}$$

We then calculate the mass flow rate along magnetic surfaces Σ as,

$$\dot{m} = \int_{\Sigma_b} \rho \frac{\mathbf{v} \cdot \mathbf{B_0}}{B} \, d\Sigma, \tag{37}$$

where Σ_b is the part of the magnetic surface within the central flux tube. Then using the equation for the elementary part of Σ which is given in (Ruderman & Petrukhin 2018) and repeated in Paper I,

$$d\Sigma = \frac{HB_0}{B} d\psi \, d\theta. \tag{38}$$

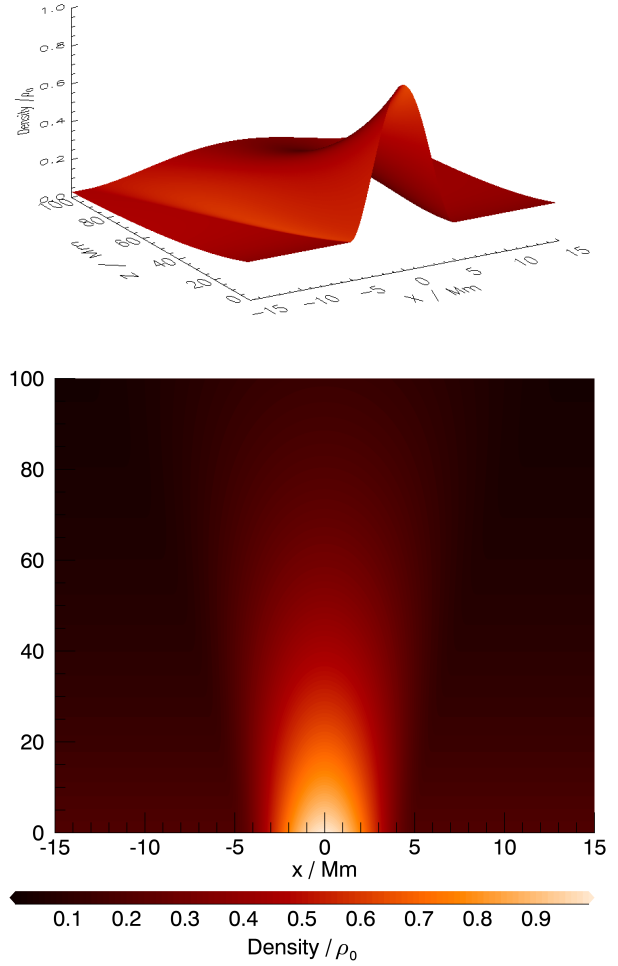we can simplify our mass flow rate calculation to,

Figure 8. A shaded surface (top) and colour contour (bottom) of the initial density across the plane $y = 0$ for the *Lare3d* simulation with $u_0 = 100$ km s^{-1}. The densities are shown in terms of the characteristic density $\rho_0 = 1.66 \times 10^{-12}$ kg m^{-3}. The density is higher within the central expanding tube structure and decreases exponentially with height.

$$\dot{m} = 2\pi HB_0 \int_0^{\psi_b} \rho \frac{\mathbf{v} \cdot \mathbf{B_0}}{B^2} \, d\psi \tag{39}$$

Using this equation we can calculate the mass flow rate through each magnetic surface. In figs. 10 and 11 we we have plotted graphs of the mass flow rate $\dot{m}$ against the height at which each corresponding magnetic surface intersects the $z-$axis. fig. 10 shows the mass flow rate for the run with $u_0 = 10$ km s^{-1} and fig. 11 shows the mass flow rate for the run with $u_0 = 100$ km s^{-1}.

The mass flow rates shown in figs. 10 and 11 are for a single point in time and we would expect the flow rates to oscillate in time with the magnetosonic waves. Note that the peak flow rate is generally larger higher up in the domain and so it would not make sense to integrate or average over the height.

We can see that for both simulations the mass flow rate in the direction of the outward magnetic field oscillates but is consistently positive over the lower domain and positive on average over the upper
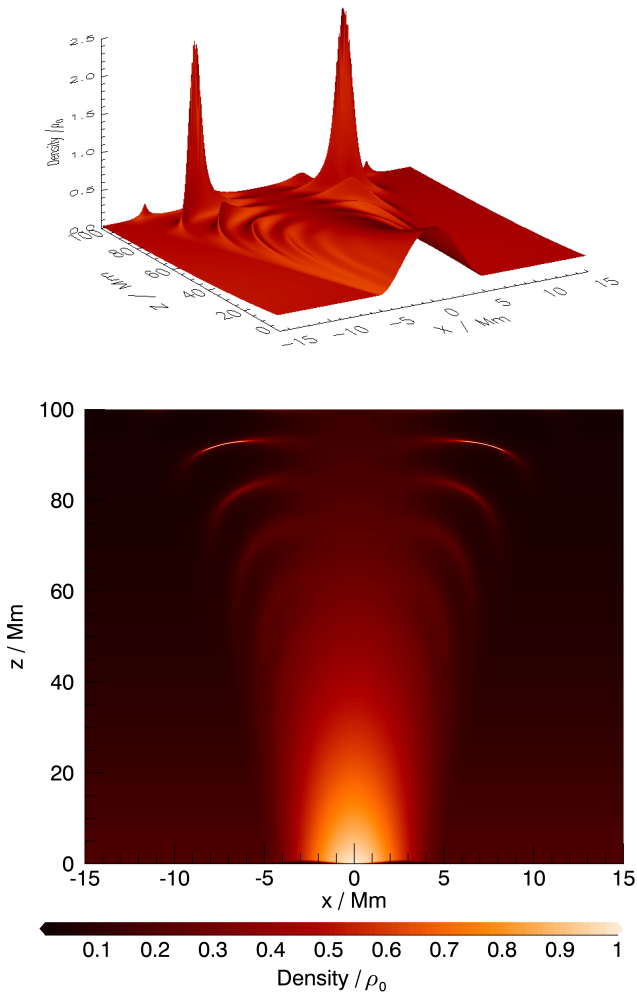
Figure 9. A shaded surface (top) and colour contour (bottom) of the density after 578 s across the plane $y = 0$ for the *Lare3d* simulation with $u_0 = 100$ km s^{-1}. The densities are shown in terms of the characteristic density $\rho_0 = 1.66 \times 10^{-12}$ kg m^{-3}. There are sharp peaks in the density higher up in the domain reaching densities of almost 2.5 ρ_0.

Figure 10. Graph of the mass flow rate $\dot{m}$ through magnetic surfaces of increasing height against the height at which each corresponding magnetic surface intersects the $z-$axis for the run with $u_0 = 10$ km s^{-1}.

Figure 11. Graph of the mass flow rate $\dot{m}$ through magnetic surfaces of increasing height against the height at which each corresponding magnetic surface intersects the $z-$axis for the run with $u_0 = 100$ km s^{-1}.

domain. As this nonlinearly induced flow is positive when averaged over an oscillation period it can be considered as an Alfvénic wind. This phenomena has also been identified in (Shestov et al. 2017) who perform similar simulations in a straight magnetic flux tube.

The flow in the lower corona is similar to peristaltic flow in compressible viscous fluids (Aarts, A. C. T. & Ooms, G. 1998), the Alfvén wave induces a net flow in the outward direction. In the upper corona the flow shows similarities to the non-Newtonian peristaltic flow, as discussed in (Tsiklauri & Beresnev 2001), with the plasma sometimes flowing inwardly, in the opposite direction to the Alfvén wave propagation. The effect of the density shocks in the $u_0 = 100$ km s^{-1} simulation can be clearly seen in fig. 11. The effect is a steepening of the leading edges of the oscillations in the upper corona and an enhancement of the positive peaks in mass flow rate, the combined effect of which is to further increase the net flow rate.
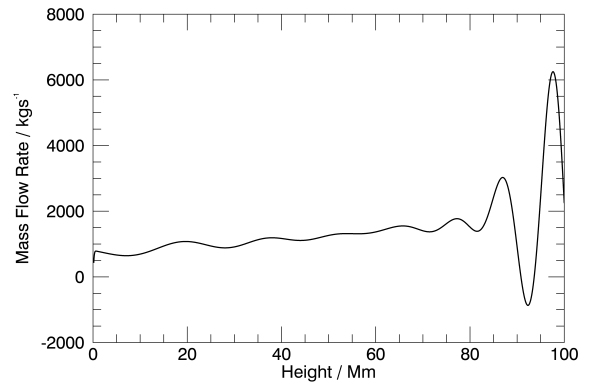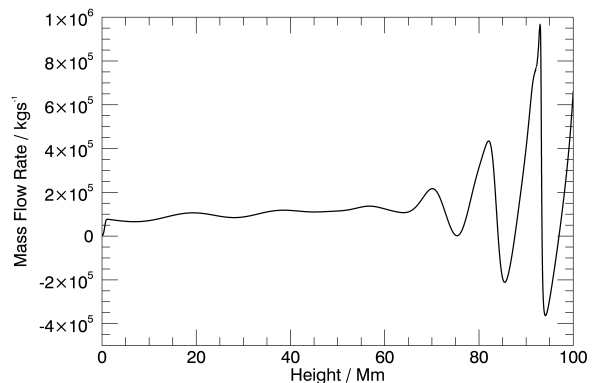
4 CONCLUSIONS

In this paper we used *Lare3d* (Arber et al. 2001), a Lagrangian remap code that solves the full viscous MHD equations over a 3D staggered Cartesian grid, to simulate the propagation of torsional Alfvén waves in a divergent and gravitationally stratified solar coronal structure. We compared the simulations outputs to those from corresponding simulations in *WiggleWave* (https://github.com/calboo/Wigglewave), a finite difference solver we developed to solve the linearised governing equations eqs. (7) and (8) directly, in order to detect nonlinear effects.

We began in section 2 by deriving the full nonlinear equations for the propagation of torsional Alfvén waves in a potential axisymmetric magnetic field. We did this to show how the linearised governing equations eqs. (7) and (8) are derived and which nonlinear terms are responsible for the generation of non-torsional and compressible perturbations. We showed that the generation of compressible magnetosonic modes by incompressible torsional Alfvén is caused by: the varying magnetic pressure of the Alfvén wave, $\nabla(\mathbf{b}^2/2\mu_0)$,

also known as the ponderomotive force; the magnetic tension force $(\mathbf{b} \cdot \nabla)\mathbf{b}/\mu_0$ and centrifugal force, $\rho_0(\mathbf{v} \cdot \nabla)\mathbf{v}$.

In section 3 we compared corresponding simulation outputs from *Lare3d* and *WiggleWave*. Comparing the torsional perturbations v_θ in figs. 3 and 4 we saw a fringed pattern superimposed onto the usual wavefront pattern in the *Lare3d* output. We also saw perturbations to v_r and v_z developing in the *Lare3d* outputs that are interpreted as magnetosonic waves excited by coupling of the Alfvén wave to magnetosonic modes. The fringed pattern in v_θ is explained as being caused by the interaction of the induced magnetosonic waves with the Alfvén wave.

Following this we ran other simulations in *Lare3d* using the same setup but with different, smaller, amplitudes for wave driving. Comparing the magnitude of magnetosonic waves in these simulations relative to the driving amplitude, as in fig. 7, we showed that the magnetosonic perturbations to v_r and v_z scale as the square of the Alfvén wave amplitude, consistent with other research on nonlinear mode coupling (Nakariakov et al. 1997; Botha et al. 2000; Shestov et al. 2017).

We then turned our attention to the compressive perturbations that are caused by the magnetosonic waves. By inspecting the density outputs from our initial *Lare3d* we can see that as the Alfvén and magnetosonic waves evolve compressive waves begin to form lower in the corona and increase in amplitude as they propagate higher up. As the waves increase in amplitude they begin to steepen and form shock waves.

By considering the mass flow rate through magnetic surfaces we also showed that the net flow is positive in the direction of the magnetic field, showing similarities to peristaltic flow in the lower corona (Aarts, A. C. T. & Ooms, G. 1998) and non-Newtonian peristaltic flow in the upper corona (Tsiklauri & Beresnev 2001). Furthermore we showed that the compressive perturbations steepen oscillations in the mass flow rate and enhance the positive peaks.

To summarise the nonlinear effects identified:

(i) The nonlinear propagation of a torsional Alfvén can excite magnetosonic waves which in turn allow the self-interaction of the Alfvén wave, this is shown in fig. 5. Mode conversion provides another possible mechanism for the viscous dissipation of Alfvén wave energy into the corona.

(ii) The longitudinal motion of the magnetosonic waves cause compressional waves in the density to form that increases in amplitude with height and steepen into shocks, as seen in fig. 9. These shock waves can be extremely efficient at dissipating heat in the corona (Malara et al. 1996).

(iii) The longitudinal motion of the magnetosonic waves causes a net flow of plasma outwardly along the magnetic field lines as shown in figs. 10 and 11. The flow includes oscillations and is not always positive in the higher corona but the positive peaks of the oscillations are enhanced by the presence of the shock waves as seen in fig. 11.

Although we were unable to quantify the rate of torsional Alfvén wave damping from our *Lare3d* simulation outputs, due to the interaction of the magnetosonic wave with the Alfvén wave, the nonlinear phenomena listed above all provide different mechanisms through which the Alfvén wave can dissipate energy. We might therefore expect greater heating rates than predicted from phase mixing alone, due to nonlinear effects in the corona.

In order to test this theory, however, further simulations must be performed in which viscous coronal heating can be accurately measured. In our current *Lare3d* simulations uniform viscosity is included only as an incompressible term in the momentum equation. If viscosity were included as a term in the energy equation then additional effects may emerge due to increased pressure at heating sites. Furthermore this may provide a method of measuring viscous heating directly.

DATA AVAILABILITY

All data used in this study was generated by either our finite difference solver *Wigglewave*, https://github.com/calboo/Wigglewave or the MHD solver *Lare3d*,(Arber et al. 2001), https://github.com/Warwick-Plasma/Lare3d.

REFERENCES

Aarts, A. C. T. Ooms, G. 1998, Journal of Engineering Mathematics, 34, 435–450

Antolin P., Shibata K., 2010, ApJ, 712, 494

Arber T., Longbottom W., Gerrard C., Milne A., 2001, Journal of Computational Physics - J COMPUT PHYS, 171, 151

Arber T. D., Brady C. S., Shelyag S., 2016, ApJ, 817, 94

Aschwanden M. J., 2004, Physics of the Solar Corona. An Introduction. Springer

Banerjee D., Teriaca L., Doyle J. G., Wilhelm K., 1998, A&A, 339, 208

Botha G. J. J., Arber T. D., Nakariakov V. M., Keenan F. P., 2000, A&A, 363, 1186

Cranmer S. R., Woolsey L. N., 2015, ApJ, 812, 71

De Moortel I., Browning P., Bradshaw S. J., Pintér B., Kontar E. P., 2008, Astronomy and Geophysics, 49, 3.21

Doyle J. G., Teriaca L., Banerjee D., 1999, A&A, 349, 956

Fletcher L., Hudson H. S., 2008, ApJ, 675, 1645

Heyvaerts J., Priest E. R., 1983, A&A, 117, 220

Hollweg J. V., 1971, J. Geophys. Res., 76, 5155

Kudoh T., Shibata K., 1999, ApJ, 514, 493

Kwatra N., Su J., Grétarsson J. T., Fedkiw R., 2009, Journal of Computational Physics, 228, 4146

Malara F., Primavera L., Veltri P., 1996, ApJ, 459, 347

Malara F., Petkaki P., Veltri P., 2000, ApJ, 533, 523

Nakariakov V., Roberts B., Murawski K., 1997, Solar Physics, 175, p.93

Ofman L., 2005, Space Sci. Rev., 120, 67

Ofman L., 2010, Journal of Geophysical Research: Space Physics, 115

Ofman L., Nakariakov V. M., DeForest C. E., 1999, ApJ, 514, 441

Parnell C. E., De Moortel I., 2012, Philosophical Transactions of the Royal Society of London Series A, 370, 3217

Roberts B., 2000, Solar Physics, 193, 139

Ruderman M. S., Petrukhin N. S., 2018, A&A, 620, A44

Shestov S. V., Nakariakov V. M., Ulyanov A. S., Reva A. A., Kuzin S. V., 2017, ApJ, 840, 64

Smith P. D., Tsiklauri D., Ruderman M. S., 2007, Astronomy & Astrophysics, 475, 1111–1123

Soler R., Terradas J., Oliver R., Ballester J. L., 2017, ApJ, 840, 20

Stangalini M., Erdélyi R., Boocock C., Tsiklauri D., Nelson C. J., Del Moro D., Berrilli F., Korsós M. B., 2021, Nature Astronomy

Tikhonchuk V. T., Rankin R., Frycz P., Samson J. C., 1995, Physics of Plasmas, 2, 501

Tsiklauri D., 2009, Astronomy and Geophysics, 50, 5.32

Tsiklauri D., Beresnev I., 2001, Phys. Rev. E, 64, 036303
Tsiklauri, D. Arber, T. D. Nakariakov, V. M. 2001, A&A, 379, 1098
Tsiklauri, D. Nakariakov, V. M. Arber, T. D. 2002, A&A, 395, 285
Vasheghani Farahani S., Nakariakov V. M., Verwichte E., Van Doorsselaere
    T., 2012, A&A, 544, A127

APPENDIX A: NONLINEAR CYLINDRICAL MHD EQUATIONS FOR PERTURBATIONS TO AN AXISYMMETRIC MAGNETOSTATIC EQUILIBRIUM

The component equations of the cold ($\beta = 0$), ideal (zero viscosity, zero resistivity) MHD equations in cylindrical coordinates, (r, z, θ), and with the condition of axisymmetry ($\partial/\partial\theta$) are as follows:

$$\rho \left[\partial_t v_r + v_r \partial_r v_r + v_z \partial_z v_r - \frac{v_\theta^2}{r} \right] = \tag{A1}$$
$$-\frac{1}{\mu_0} \left(\frac{B_\theta}{r} \partial_r (r B_\theta) - B_z \left(\partial_z B_r - \partial_r B_z \right) \right),$$

$$\rho \left[\partial_t v_\theta + \left(v_r \partial_r v_\theta + v_z \partial_z v_\theta + \frac{v_\theta v_r}{r} \right) \right] = \tag{A2}$$
$$-\frac{1}{\mu_0} \left(-B_r \frac{1}{r} \partial_r (r B_\theta) - B_z \partial_z B_\theta \right),$$

$$\rho \left[\partial_t v_z + v_r \partial_r v_z + v_z \partial_z v_z \right] = \tag{A3}$$
$$-\frac{1}{\mu_0} \left(B_\theta \partial_z B_\theta - B_r \left(\partial_r B_z - \partial_z B_r \right) \right),$$

$$\partial_t B_r = -\partial_z \left(v_z B_r - v_r B_z \right), \tag{A4}$$

$$\partial_t B_\theta = \partial_z \left(v_\theta B_z - v_z B_\theta \right) - \partial_r \left(v_r B_\theta - v_\theta B_r \right), \tag{A5}$$

$$\partial_t B_z = \frac{1}{r} \partial_r \left(r v_z B_r - r v_r B_z \right), \tag{A6}$$

$$\partial_t \rho + \frac{1}{r} \partial_r (r \rho v_r) + \partial_z (\rho v_z) = 0. \tag{A7}$$

If we now consider perturbations to an equilibrium state, $\mathbf{v_0} = \mathbf{0}$, $\mathbf{B_0} = (B_{0r}, 0, B_{0z})$ and $\rho_0 = \rho_0(r, z)$, that take the form,

$$\begin{aligned} \rho &= \rho_0 + \rho', \\ \mathbf{v} &= \mathbf{0} + \mathbf{v}, \\ \mathbf{B} &= \mathbf{B_0} + \mathbf{b}, \end{aligned} \tag{A8}$$

where our equilibrium magnetic field is a potential field such that,

$$\nabla \times \mathbf{B_0} = \begin{pmatrix} 0 \\ \partial_z B_{0r} - \partial_r B_{0z} \\ 0 \end{pmatrix} = \mathbf{0}. \tag{A9}$$

then our equations become,

$$\rho_0 \partial_t v_r - \frac{B_{0z}}{\mu_0} \left(\partial_z b_r - \partial_r b_z \right) = N_1, \tag{A10}$$

$$\rho_0 \partial_t v_\theta - \frac{1}{\mu_0} \left(\frac{B_{0r}}{r} \partial_r (r b_\theta) + B_{0z} \partial_z b_\theta \right) = N_2, \tag{A11}$$

$$\rho_0 \partial_t v_z - \frac{B_{0r}}{\mu_0} \left(\partial_r b_z - \partial_z b_r \right) = N_3, \tag{A12}$$

$$\partial_t b_r + \partial_z \left(B_{0r} v_z - B_{0z} v_r \right) = N_4, \tag{A13}$$

$$\partial_t b_\theta - \left(\partial_z \left(B_{0z} v_\theta \right) + \partial_r \left(B_{0r} v_\theta \right) \right) = N_5, \tag{A14}$$

$$\partial_t b_z - \frac{1}{r} \partial_r \left(r B_{0r} v_z - r B_{0z} v_r \right) = N_6, \tag{A15}$$

$$\partial_t \rho' + \partial_r \left(r \rho_0 v_r \right) + \partial_z \left(\rho_0 v_z \right) = N_7, \tag{A16}$$

where all the linear terms are on the LHS and all the nonlinear terms are on the RHS. The nonlinear terms are,

$$\begin{aligned} N_1 = &-\rho' \partial_t v_r - (\rho_0 + \rho') \left[v_r \partial_r v_r + v_z \partial_z v_r + \frac{v_\theta^2}{r} \right] \\ &- \frac{1}{\mu_0} \left(b_\theta \partial_r b_\theta - b_z \left(\partial_z b_r - \partial_r b_z \right) + \frac{b_\theta^2}{r} \right), \end{aligned} \tag{A17}$$

$$\begin{aligned} N_2 = &-\rho' \partial_t v_\theta - (\rho_0 + \rho') \left[v_r \partial_r v_\theta + v_z \partial_z v_\theta + \frac{v_\theta v_r}{r} \right] \\ &+ \frac{1}{\mu_0} \left(b_r \partial_r b_\theta + b_z \partial_z b_\theta + \frac{b_r b_\theta}{r} \right), \end{aligned} \tag{A18}$$

$$\begin{aligned} N_3 = &-\rho' \partial_t v_z - (\rho_0 + \rho') \left[v_r \partial_r v_z + v_z \partial_z v_z \right] \\ &- \frac{1}{\mu_0} \left(b_\theta \partial_z b_\theta - b_r \left(\partial_r b_z - \partial_z b_r \right) \right), \end{aligned} \tag{A19}$$

$$N_4 = -\partial_z \left(v_z b_r - v_r b_z \right), \tag{A20}$$

$$N_5 = \partial_z \left(v_\theta b_z - v_z b_\theta \right) + \partial_r \left(v_\theta b_r - v_r b_\theta \right), \tag{A21}$$

$$N_6 = \frac{1}{r} \partial_r \left(r v_z b_r - r v_r b_z \right), \tag{A22}$$

$$N_7 = -\frac{1}{r} \partial_r \left(r \rho' v_r \right) - \partial_z \left(\rho' v_z \right). \tag{A23}$$

These are the nonlinear cylindrical equations for perturbations to the axisymmetric magnetostatic equilibrium. We can see from these equations that the nonlinear terms, N_1, N_3, N_4 and N_6 which correspond to the evolution equations for v_r, v_z, b_r and b_z, contain terms with either two magnetosonic variables or two Alfvén wave variables, indicating that the magnetosonic waves can be excited by Alfvén waves and can self-interact. In contrast the nonlinear terms, N_2 and N_5, that correspond to the evolution equations for v_θ and b_θ, contain only terms with an Alfvén wave variable and a magnetosonic variable, indicating that they cannot be excited by magnetosonic waves but can interact with the induced magnetosonic waves.

APPENDIX B: LINEARISED EQUATIONS FOR TORSIONAL ALFVÉN WAVES IN A POTENTIAL AXISYMMETRIC MAGNETIC FIELD

Looking at the equations in appendix A we can see that, if the nonlinear terms are ignored, then setting v_r, b_r, v_z, b_z and $\rho' = 0$ results in an incompressible system with only torsional perturbations. The equations become,

$$\rho_0 \partial_t v_r = 0, \tag{B1}$$

$$\rho_0 \partial_t v_\theta = \frac{1}{\mu_0} \left(\frac{B_{0r}}{r} \partial_r (r b_\theta) + B_{0z} \partial_z b_\theta \right), \tag{B2}$$

$$\rho_0 \partial_t v_z = 0, \tag{B3}$$

$$\partial_t b_r = 0, \tag{B4}$$

$$\partial_t b_\theta = \partial_z (B_{0z} v_\theta) + \partial_r (B_{0r} v_\theta), \tag{B5}$$

$$\partial_t b_z = 0, \tag{B6}$$

$$\partial_t \rho' = 0. \tag{B7}$$

This system remains incompressible and perturbations remain purely torsional, i.e. only in v_θ and b_θ. The equations for v_θ and b_θ can then be simplified as follows,

$$
\begin{aligned}
\rho_0 \partial_t v_\theta &= \frac{1}{\mu_0} \left(\frac{B_{0r}}{r} \partial_r (r b_\theta) + B_{0z} \partial_z b_\theta \right) \\
&= \frac{1}{r \mu_0} \left(B_{0r} \partial_r (r b_\theta) + B_{0z} \partial_z (r b_\theta) \right) \\
&= \frac{1}{r \mu_0} \left(\mathbf{B_0} \cdot \nabla (rb) \right),
\end{aligned} \tag{B8}
$$

$$
\begin{aligned}
\partial_t b_\theta &= \partial_z (B_{0z} v_\theta) + \partial_r (B_{0r} v_\theta) \\
&= B_{0r} \partial_r v_\theta + B_{0z} \partial_z v_\theta + v_\theta (\partial_r B_{0r} + \partial_z B_{0z}) \\
&= B_{0r} \partial_r v_\theta + B_{0z} \partial_z v_\theta - \frac{v_\theta B_{0r}}{r} \\
&= r \left(\mathbf{B_0} \cdot \nabla \left(\frac{v}{r} \right) \right),
\end{aligned} \tag{B9}
$$

where we have used Gauss' law for magnetism,

$$
\begin{aligned}
\nabla \cdot \mathbf{B_0} &= 0, \\
\Rightarrow \quad \partial_r B_{0r} + \partial_z B_{0z} &= -\frac{B_{0r}}{r},
\end{aligned} \tag{B10}
$$

if we reintroduce the viscosity term then we have the same linearised governing equations presented in Paper I,

$$\rho \frac{\partial v}{\partial t} = \frac{1}{r \mu_0} \left(\mathbf{B_0} \cdot \nabla (rb) \right) + \frac{1}{r} \frac{\partial}{\partial r} \left(\rho \nu r \frac{\partial v}{\partial r} \right) + \frac{\partial}{\partial z} \left(\rho \nu \frac{\partial v}{\partial z} \right), \tag{B11}$$

$$\frac{\partial b}{\partial t} = r \mathbf{B_0} \cdot \nabla \left(\frac{v}{r} \right). \tag{B12}$$

This paper has been typeset from a TeX/LaTeX file prepared by the author.